

Thickness-Dependent Permeance of Molecular Layer-By-Layer Polyamide Membranes

William D. Mulhearn, Vladimir P. Oleshko, Christopher M. Stafford

Materials Science and Engineering Division, National Institute of Standards and Technology,
Gaithersburg, MD 20899, USA

ABSTRACT

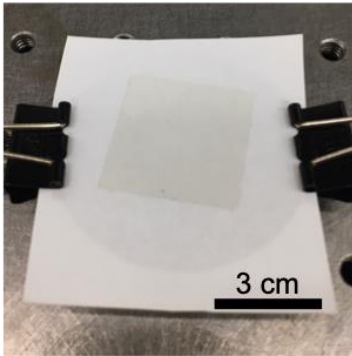
We present the thickness-dependent permeance of highly cross-linked polyamide (PA) membranes formed by a molecular layer-by-layer (mLbL) deposition process. The deposition allows for the synthesis of extremely smooth, uniform PA films of tunable thickness, which is counter to the less controlled interfacial polymerization process used commercially. The ability to control and measure the membrane thickness allows us to elucidate the relationships among network structure, transport properties, and separation performance. In this work, a series of large-area mLbL PA membranes is prepared with thickness ranging from less than 5 nm to greater than 100 nm, which can be transferred defect-free via a film floating technique onto a macroporous support layer and challenged with salt solutions. A critical thickness of 15 nm is identified for efficient desalination, and water permeance is described using a multi-layer solution diffusion model that allows for the extraction of material properties relevant to transport. Finally, the model demonstrates the existence of two distinct layers in the mLbL films, one layer comprised of a (5 to 10) nm graded or less cross-linked layer at the surface and a more densely cross-linked layer in the interior of the film. This graded layer appears inherent to the mLbL deposition process and is observed at all film thicknesses.

TOC Graphic

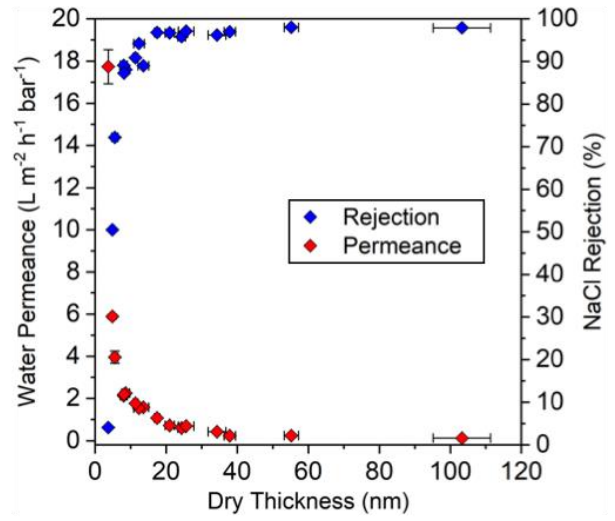
polyamide (5–100 nm)

PSS

substrate



film floating



1. Introduction

Membrane-based reverse osmosis (RO) has been established as the prevailing method for water desalination and wastewater treatment,[1,2] due in large part to decades of work towards improving the energy efficiency of membrane separation processes.[3] As stress on the clean water supply continues to mount worldwide,[4] optimization of these membranes to allow greater throughput and separation efficiency is critical. To meet this challenge, engineers require a deeper understanding of the fundamental transport properties of the materials at the core of the separation.

Commercial RO membranes are prepared as a thin-film composite via interfacial polymerization (IP) of an acid chloride, *e.g.*, trimesoyl chloride (TMC), and a diamine, *e.g.*, *m*-phenylenediamine (MPD) atop a macroporous polymer layer to impart mechanical support.[1,2,5] The resulting (100 to 200) nm thick cross-linked polyamide (PA) selective layer has an extremely rough ridge-and-valley structure[6] and exhibits depth heterogeneities in density and distribution of polar functional groups owing to the complexities of the diffusion-restricted IP reaction process.[7–9] As such, it is difficult to interpret the results of membrane performance testing – measurements of solution flux and solute rejection – in such a way that the influence of intrinsic material properties can be cleanly disentangled from the influence of large-scale morphological irregularities arising from the polymerization process. For example, perhaps the most common analytical model for describing transport through a non-porous polymer membrane is the solution-diffusion (SD) model.[10,11] The SD model has been widely applied to RO membranes with great success, but always with the caveats that the membrane is approximated as a slab of uniform thickness despite IP membranes often having root mean square roughness comparable to the average total thickness,[12] and that the material properties

derived from the model represent an average across the heterogeneous path traversed by the solution as it permeates through the membrane.

Molecular layer-by-layer (mLbL) deposition enables the preparation of PA membranes in a highly controlled manner, such that mLbL films have been reported with surface roughness nearly two orders of magnitude lower than those typical of the IP process[13] and with film thickness readily tailored via the number of monomer deposition cycles. As IP typically generates PA membranes with thicknesses greater than 100 nm, there has been growing interest in synthesizing ultrathin membranes as a means to improve solution flux. Recent work has successfully demonstrated the synthesis of ultrathin (< 15 nm) PA films via a controlled IP process, with greatly improved solution flux relative to their thicker counterparts prepared via conventional IP.[14,15] The mLbL method also provides a direct synthetic route to the production of extremely thin membranes with improved performance. For example, macroporous polyacrylonitrile (PAN) support layers have been primed for mLbL by coating with a thin polyelectrolyte film to block polymerization from occurring within the supporting PAN pore network,[16,17] or by pre-functionalization with diethylenetriamine[18] followed by TMC/MPD mLbL deposition directly onto the support. These mLbL membranes exhibit efficient solute rejection at thicknesses of only a few tens of nanometers, with the low hydraulic resistance of such thin active layers permitting rapid solution transport.

In the present work mLbL films were prepared on silicon wafers pre-coated with a water-soluble poly(sodium 4-styrene sulfonate) (PSS) release layer, and portions of the mLbL films were subsequently transferred defect-free either onto the PAN support or onto another testing medium. This two-stage process has the advantage of permitting more comprehensive *ex situ* characterization of portions of the same specimens used for performance testing – enabling direct

quantification of thickness and small-scale morphology – than if the film were prepared on and thus tightly bonded to the PAN layer. By combining these precise measurements of membrane thickness with those of solution transport through the membrane using a well-controlled model system, we can approach the problem of extracting material properties in a much more rigorous fashion than would be possible otherwise.

2. Experimental

2.1. Materials

Equipment and materials are identified in the article to adequately specify the experimental details. Such identification does not imply recommendation by the National Institute of Standards and Technology, nor does it imply that the materials are necessarily the best available for the purpose. TMC monomer, MPD monomer, and aqueous PSS solution (15 % mass fraction in water) were purchased from Sigma Aldrich and were used as received. Toluene was dried over 3 Å molecular sieves and tetrahydrofuran (THF) was dried using a solvent purification system (LC Technology Solutions), both to water content of less than 25 ppm (<25 mg/kg of water) as measured on a Karl Fisher CS20X coulometric titrator (Mettler Toledo). Silicon wafer substrates were cleaned by sequential rinses with toluene, ethanol, and deionized water (Barnstead Nanopure, 18 MΩ/cm), followed by ultraviolet ozone treatment for 20 min. PAN ultrafiltration membranes (PAN50) were purchased from Sepro Membranes, Inc. 3-aminopropyltrimethylethoxysilane (APDES) was purchased from Gelest and used as received. Commercial FilmTec BW30XLE membranes were kindly provided by Dupont Water Solutions.

2.2. Membrane Synthesis

In all cases except one, cleaned silicon wafers to be used as PA synthesis substrates were coated with ≈ 50 nm PSS films by spin coating PSS solutions, diluted to 2 % mass fraction in water, at 2000 rpm (209 rad/s). These coated wafers were heated to 70 °C under vacuum for at least 1 h to minimize residual moisture. In the remaining case, the cleaned silicon wafer was not coated with PSS but was instead immersed in a 2 % solution by mass of APDES in toluene at 35 °C for 24 h followed by a toluene rinse, to promote covalent bonding between the PA film and the substrate.

Monomer solutions were prepared of 0.4 % by mass of TMC in toluene and 0.4 % by mass of MPD in toluene. Solutions were loaded into gas-tight syringes and deposited through 0.45 μ m syringe filters onto the substrate inside an environmental spin coater (Laurell Technologies) purged with dry air to minimize exposure to water.[19] One deposition cycle consisted of sequential deposition onto the substrate and spinning dry of the TMC monomer solution, pure toluene rinse solvent, the MPD monomer solution, and finally pure THF rinse solvent. The film thickness could be tailored by controlling the number of deposition cycles, with the average film growth rate corresponding to approximately 0.4 nm/cycle.

2.3. Membrane Characterization

The dry thickness of the PA samples deposited onto PSS-coated substrates was characterized via ellipsometry using a variable angle spectroscopic ellipsometer (J.A. Woollam). Thicknesses were acquired following two methods. In the first method, the PSS release layer was measured prior to mLbL deposition and then retained as an input for measurement of the PA/PSS bilayer after synthesis, as it was found that the PSS films did not measurably change upon cyclic exposure to toluene and THF in the environmental spin coater. In the second method, a portion

of the synthesized PA film was floated onto the surface of a water bath by dissolving the sacrificial release layer (PSS) and recovered on a clean silicon wafer, dried under vacuum, and measured as a single layer. These two methods showed very good agreement, indicating that the floating process did not appreciably distort the films and that the amount of water-extractable material in the films (*e.g.*, unreacted monomer) was minimal.

The thickness of the PA sample deposited onto the APDES-treated substrate (180 deposition cycles) was characterized using a fixed-angle spectroscopic ellipsometer (J.A. Woollam) equipped with a sealed vapor cell. The dry film thickness first was measured while purging with dry air, and the film was then allowed to equilibrate with saturated toluene vapor for 18 h during measurement to determine the equilibrium thickness in the toluene-swollen state.

Tapping mode atomic force microscopy (AFM) images were collected on a Dimension Icon (Bruker Nano Surfaces) using TAP525 probes with a nominal spring constant of 200 N/m and a nominal radius of curvature of 8 nm. PA films were floated onto cleaned silicon wafers and dried under vacuum prior to imaging via AFM.

Medium and high-resolution transmission electron microscopy (TEM) imaging of the PA films was performed in a Schottky field-emission FEI Titan 80–300 S/TEM (Thermo Fischer Scientific) with a point-to-point resolution of 0.19 nm and information limit below 0.1 nm, equipped with a S-TWIN objective lenses and operating at 300 kV accelerating voltage. PA films were floated onto lacey carbon films supported by 200 mesh microscopy Cu grids, and images were recorded using a 2048×2048 pixel Ultrascan digital charge coupled device (CCD) camera (Gatan). To reduce beam-induced damage of the specimens, the electron beam dose rates were minimized down to $4.5 \text{ e/nm}^2/\text{s}$ and beam blanking was employed between acquisitions during imaging.

2.4. Performance Testing

To facilitate desalination performance testing, the PA films were transferred onto a PAN support layer. A PAN ultrafiltration membrane was chosen as the support material for consistency with prior work on the transport properties and performance of mLbL membranes.[16,20,21] The edges of a 4 cm × 4 cm wafer piece, coated with the PA film and PSS release layer, were scored to ease film floating and slowly lowered into a deionized water bath at a shallow angle to avoid tearing the film as it releases from the wafer. Prior to floating the mLbL film, a PAN support was clipped flat to a porous metal plate and positioned at the bottom of the water bath. The water was then drained from a valve at the bottom of the water bath, lowering the PA film gently onto the PAN layer. Due to the lack of covalent bonding between the PA film and the PAN support, the films were allowed to thoroughly dry overnight to promote adhesion prior to trimming and mounting in the testing apparatus. Membrane performance was tested against ≈1000 mg/L NaCl aqueous solutions in a stirred dead-end filtration cell (HP4750, Sterlitech). The active membrane area was 4.16 cm² and the operating pressure was 34.5 bar (500 psi, or 3.45 MPa).[22] This high operating pressure was necessitated by the low solution permeance of the thickest membranes in the series. Salt concentrations were determined using an Orion 3 Star Plus conductivity meter (Thermo Scientific).

3. Results and Discussion

3.1. Membrane Morphological Characterization

A series of 17 TMC/MPD films were prepared with thicknesses ranging from less than 5 nm to greater than 100 nm, following the scheme shown in Figure 1. Throughout this range, the

films remain smooth and exhibit a consistent growth rate of approximately 0.40 nm per deposition cycle. A plot of film thickness vs. number of deposition cycles is provided in the Supporting Information. This growth rate is consistent with atomistic simulations of TMC/MPD mLbL deposition, which suggest growth rates between 0.2 nm per cycle and 0.8 nm per cycle depending on synthetic conditions.[23] Our measured growth rate is closer to the lower end of this range, and experimental growth rates as high as ≈ 1 nm per cycle have been previously reported in systems with different rinse solvents;[24] we attribute our relatively low growth rate to efficient removal of unreacted monomers due to our choice of THF rinse solvent.

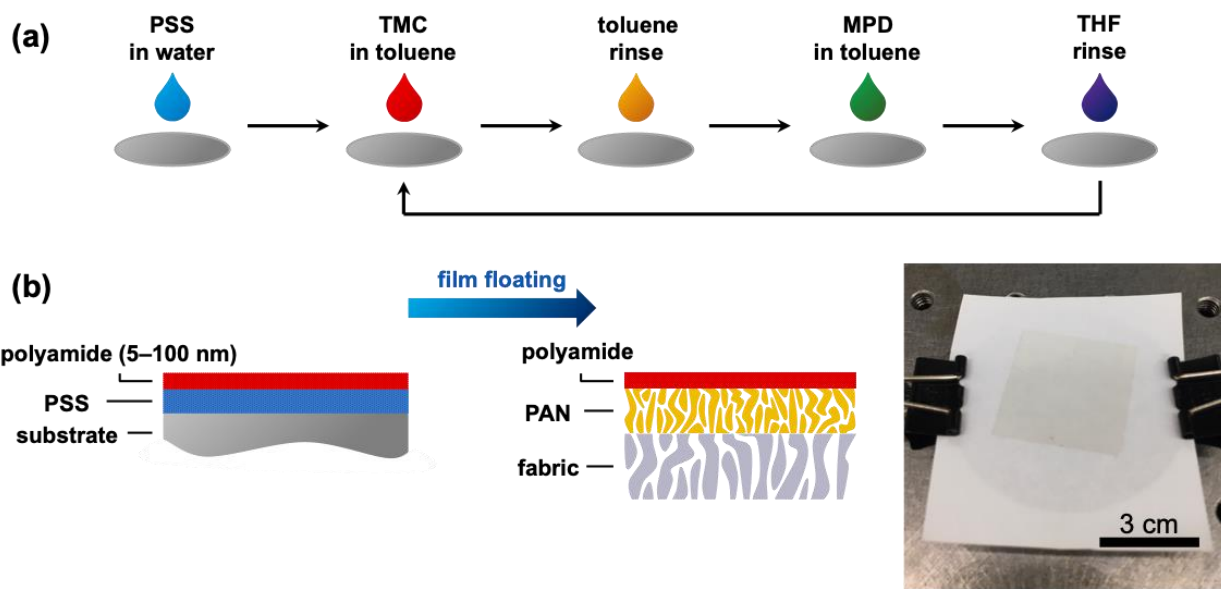


Figure 1. (a) Schematic diagram of release layer and mLbL deposition on silicon substrate. (b) Procedure for floating an mLbL PA film from the deposition substrate onto a macroporous PAN support layer. The final PA/PAN bilayer is shown in the image on the right.

The surface morphology and roughness of the films were characterized by AFM; examples of a thin film, an intermediate film, and a thick film from this range are shown in

Figure 2. The images are shown with a common height scale of (0 to 12) nm, to emphasize variations in the average size of surface features among the three films. Each film surface exhibits a globular structure, with structures on the scale of tens of nm in diameter and up to 10 nm in height for the thickest film. These surface features may imply a growth pattern analogous to the cluster-cluster aggregation model proposed for IP PA network formation,[25,26] which gives rise to locally heterogeneous structures. Despite the potential complexities of the growth pattern, the films remain smooth and continuous throughout the thickness range investigated here. The thin film (Figure 2a) has an average dry thickness of 9 nm and a root mean square (rms) roughness of 0.8 nm, the intermediate film (2b) has an average dry thickness of 33 nm and rms roughness of 1.0 nm, and the thick film (2c) has an average dry thickness of 55 nm and rms roughness of 1.3 nm. Thus, although the globular surface structures clearly coarsen as the films grow, the rms surface roughness as a percentage of the total thickness decreases across this series from 9 % to 2 %. Therefore, these films can be well approximated as uniform sheets without the complicated ridge-and-valley morphology typical of an IP membrane.[6] For comparison, a typical commercial RO membrane synthesized via IP exhibits rms roughness of (170 ± 30) nm, a value comparable to the total membrane thickness.[13]

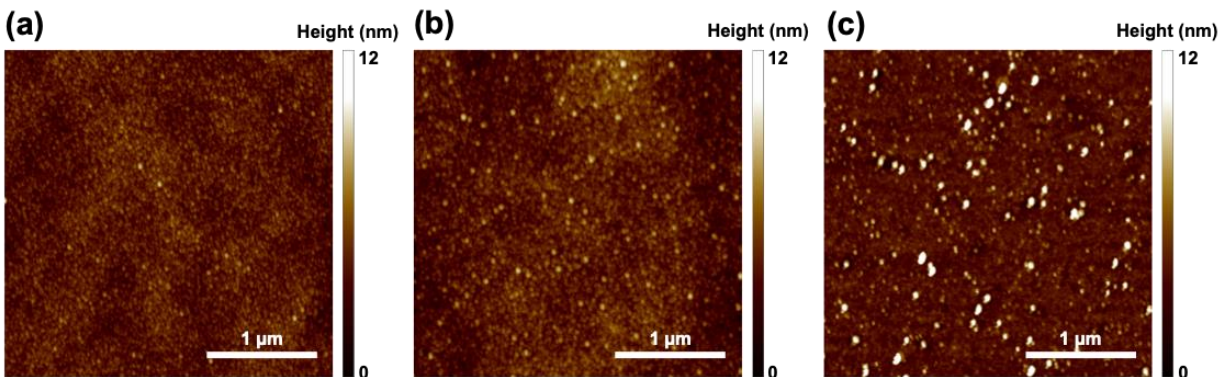


Figure 2. Tapping mode AFM of TMC/MPD mLbL films after floating and picked up on clean Si wafers. (a) 25 deposition cycles, dry thickness 9 nm, rms roughness 0.8 nm, (b) 90 deposition cycles, dry thickness 33 nm, rms roughness 1.0 nm, (c) 150 deposition cycles, dry thickness 55 nm, rms roughness 1.3 nm.

A portion of the thinnest film from this series was characterized via TEM to verify that sufficient material had been deposited to generate a dense, non-porous network. Representative large-area bright-field TEM and high-resolution TEM images are shown in Figure 3. The high-resolution image (Fig 3a) reveals a continuous, dense film, although weak, randomly distributed contrast variations are apparent over a ≈ 5 nm length scale. The visible features are smaller than the analogous globular structures visible by AFM, but similarly suggest some degree of monomer aggregation during the deposition process. Over a somewhat larger length scale (Fig 3b), the large-area image shows an essentially featureless sheet lacking any discernable channels through the membrane thickness.

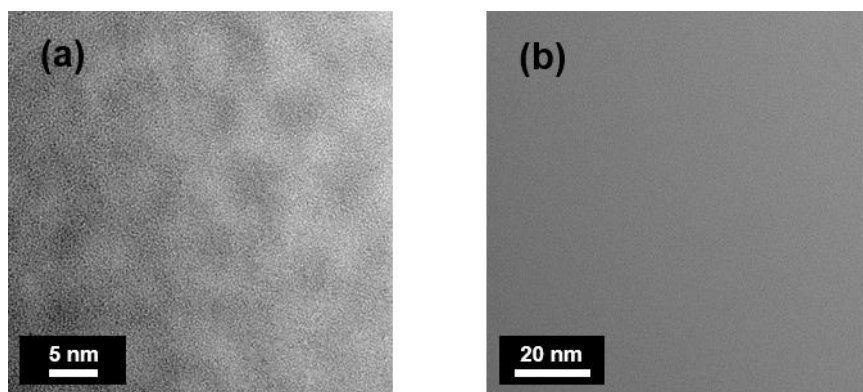


Figure 3. Electron microscopy images of a freestanding TMC/MPD mLbL film (15 deposition cycles, dry thickness 4 nm): (a) high-resolution bright field TEM image, and (b) large-area bright field TEM image.

3.2. Membrane Desalination Performance

NaCl desalination performance testing was carried out on each of the 17 PA samples in a stirred dead-end geometry. The performance metrics of interest are water flux, J_w , and solute rejection, R . The measured water flux is divided by the difference between the applied pressure, $\Delta P = 34.5$ bar, and the osmotic pressure difference across the membrane at the time of collection, $\Delta\pi = (0.80 \text{ to } 0.95)$ bar, to give the water permeance. The solute rejection is defined as,

$$R = \left(1 - \frac{c_p}{c_f}\right) \times 100 \%$$

(1)

where c_f and c_p are the NaCl concentrations of the feed (*i.e.* concentrated solution within the dead-end cell) and of the permeate, respectively. The feed NaCl concentration and osmotic pressure are recalculated at each time of collection, based on the total volumes and concentrations of the collected permeate solution. It is assumed that the stirred cell minimizes the effects of concentration polarization at the membrane surface, and therefore these effects are excluded from the performance calculations.

For each membrane, permeate aliquots were collected until the water permeance and NaCl rejection stabilized, typically over the span of a few hours. An example, the time-dependent permeance and rejection for a 34 nm film are shown in Figure 4. Permeance rapidly decreases from its initial value to a stable value, while rejection asymptotically increases over a somewhat longer time scale. These trends are consistent with compaction of the membrane under pressurized operation.[27,28]

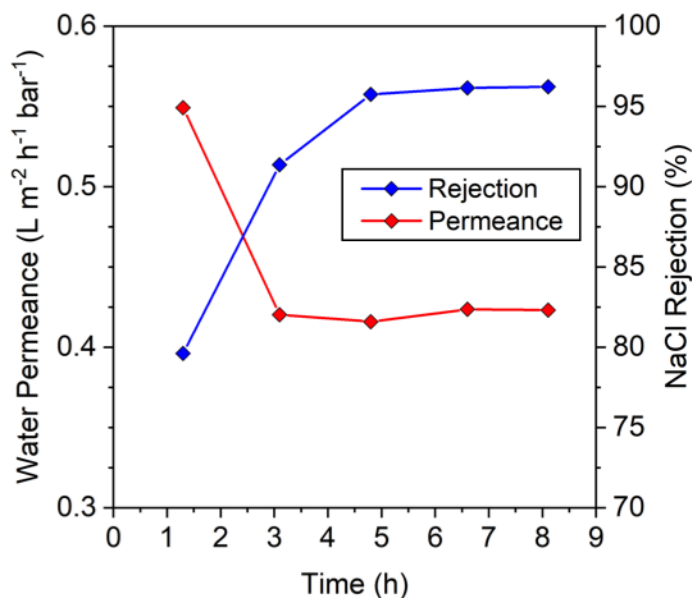


Figure 4. Stabilization of water permeance and NaCl rejection over time for a TMC/MPD mLbL membrane (100 deposition cycles, dry thickness 34 nm) on a PAN support. Applied pressure $\Delta P = 34.5$ bar, and initial feed concentration $c_{f,0} = 1000$ mg/L NaCl.

The compiled results of stirred dead-end desalination performance testing on the 17 TMC/MPD films are shown in Figure 5. For comparison, a bare PAN50 macroporous layer with no PA membrane has a water permeance of $620 \text{ L m}^{-2} \text{ h}^{-1} \text{ bar}^{-1}$, measured at $\Delta P = 6.9$ bar. The data exhibit the expected tradeoff between flux and solute rejection: at low thickness the membranes permit fast transport but cannot effectively exclude solvated ions, while at higher thickness separation is enhanced at the cost of decreased flux. A critical transition seems to occur at a dry selective layer thickness of (8 to 15) nm; below this band NaCl rejection is strongly dependent on thickness and approaches 0 % for the thinnest film (4 nm), while above this range NaCl rejection is high (96 % or greater) and is independent of thickness. This critical thickness range could have one of several explanations: very thin films may lack mechanical stability against pressure and rupture during operation, they may still contain a degree of sub-nanometer

porosity to allow salt passage (although such pores are invisible by TEM), or they may lack sufficient cross-link density to maintain a tight network structure. These possibilities are evaluated in the conclusion, informed by the following discussion of solution transport.

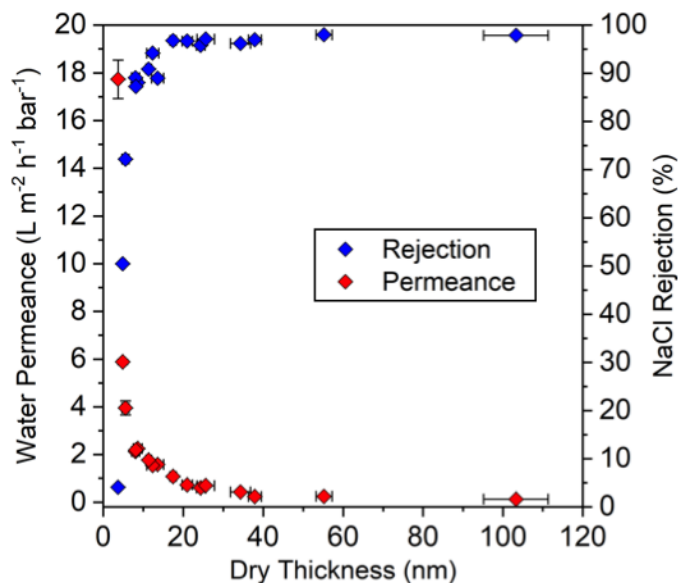


Figure 5. Water permeance and NaCl rejection vs. thickness for TMC/MPD mLbL membranes on PAN supports. The error bars represent one standard deviation of the data ($n = 3$ to 5), which is taken as the experimental uncertainty of the measurement. Some error bars are smaller than the symbols. Applied pressure $\Delta P = 34.5$ bar, and initial feed concentration $c_{f,0} \approx 1000$ mg/L NaCl.

In terms of performance for a practical desalination process, the minimum effective layer thickness for this chemistry under these preparation conditions is approximately 15 nm. Membranes of this thickness are capable of high NaCl rejection required of RO and exhibit water permeance of ≈ 1.5 L m⁻² h⁻¹ bar⁻¹. For comparison, typical water permeance reported for commercial RO and brackish water membranes range from ≈ 1 L m⁻² h⁻¹ bar⁻¹ to ≈ 4 L m⁻² h⁻¹ bar⁻¹, for apparent active layer PA thicknesses greater than 100 nm.[15] This range is consistent with

a control measurement we performed on a DuPont FilmTec XLE brackish water membrane in our stirred dead-end geometry, which equilibrated to water permeance of $(3.6 \pm 0.1) \text{ L m}^{-2} \text{ h}^{-1} \text{ bar}^{-1}$ with NaCl rejection of $(97.5 \pm 0.1) \%$. The greater flux per thickness of the IP membranes relative to mLbL membranes may be attributable to the complex depth-heterogeneity that arises from the IP process. The salt rejection and much of the hydraulic resistance may arise from a dense PA barrier layer no larger than 20 nm in thickness, which lines a much thicker and looser PA ridge and protuberance structure.[29,30] The mLbL process likely generates films with a significantly higher cross-link density and less free volume than their IP counterparts, which restricts the diffusion of solvents. Furthermore, IP membranes may exhibit higher overall fluxes than their mLbL counterparts due to their much greater surface roughness, which presents a larger available surface area for water to partition into the active layer.[31]

3.3. Modeling Solution Transport

As the active layers of RO membranes are non-porous, transport in these systems is conventionally described by means of the solution-diffusion (SD) model.[2,10] Here, the diffusion of species i follows Fick's law,

$$J_i = -\frac{D_i c_i}{RT} \frac{\partial \mu_i}{\partial z} \quad (2)$$

where D_i is the species diffusion coefficient, c_i is the molar concentration, μ_i is the chemical potential, z is the distance coordinate along the transport axis, R is the gas constant, and T is the absolute temperature. The chemical potential is defined relative to a reference state,

$$\mu_i = \mu_{i,0} + RT \ln(\gamma_i c_i) + v_i (P - P_0) \quad (3)$$

where γ_i is the activity coefficient, v_i is the molar volume ($v_w = 1.8 \times 10^{-5} \text{ m}^3/\text{mol}$ for water), and P is the pressure. The pressure and the material properties D_i and γ_i are assumed to be constant

throughout the membrane, with the membrane pressure equal to the feed pressure, P_f . Eqn. 2 can then be integrated across the membrane thickness to yield,

$$J_i = \frac{D_{i,m}}{h_m} (c_{i,m,hi} - c_{i,m,lo}) \quad (4)$$

where h_m is the membrane thickness, and $c_{i,m,hi}$ and $c_{i,m,lo}$ are the species concentrations within the membrane at the high-concentration interface (*i.e.*, feed side) and the low-concentration interface (*i.e.*, permeate side), respectively. The subscript m denotes quantities inside the membrane. Although the SD model describes a dynamic process, equilibrium is assumed for the diffusing species across the interfaces with the feed and with the permeate. Matching chemical potentials across the interface gives,

$$J_i = \frac{D_{i,m}}{\gamma_{i,m} h_m} (\gamma_{i,f} c_{i,f} - \gamma_{i,p} c_{i,p} e^{-v_i \Delta P / (RT)}) \quad (5)$$

where the subscripts f and p refer to the feed and the permeate, respectively, and $\Delta P = P_f - P_p$.

For the dilute solutions considered here, the activity coefficients of the feed and permeate can be taken to be unity and eqn. 5 can be rewritten as,

$$J_i = \frac{D_{i,m} c_{i,f}}{\gamma_{i,m} h_m} (1 - e^{-v_i (\Delta P - \Delta \pi) / (RT)}) \quad (6)$$

where the osmotic pressure difference is,

$$\Delta \pi = \frac{RT}{v_i} \ln \left(\frac{c_{i,p}}{c_{i,f}} \right) \quad (7)$$

Finally, eqn. 6 can be well approximated as,

$$J_i \approx \frac{D_{i,m} c_{i,f} v_i}{RT \gamma_{i,m} h_m} (\Delta P - \Delta \pi) \quad (8)$$

The SD model therefore predicts that, for a series of RO experiments in which the membrane material, solution, and operating pressure are identical, the measured water flux should be inversely proportional to the membrane thickness, with the proportionality constant containing the quotient of the two membrane material properties of interest, $D_{w,m} / \gamma_{w,m}$. Figure 6a

shows a best fit of the measured permeance to eqn. 8, corresponding to $D_{w,m} / \gamma_{w,m} = 5.9 \times 10^{-12}$ m²/s. Assuming for illustration 10 % membrane swelling in equilibrium with water of activity 1, a typical value for intermediate-thickness mLbL PA films,[32] we can estimate a water activity coefficient within the membrane of $\gamma_{w,m} \approx 11$ and therefore $D_{w,m} \approx 6.5 \times 10^{-11}$ m²/s. This value is two orders of magnitude less than the water self-diffusion coefficient measured at 25 °C by pulsed magnetic field gradient NMR, $D_w = 2.3 \times 10^{-9}$ m²/s.[33] Figure 6b shows a point-by-point calculation of the material parameter $D_{w,m} / \gamma_{w,m}$. There is a strong thickness dependence, with thicker films exhibiting monotonically lower values of $D_{w,m} / \gamma_{w,m}$, indicating restricted transport. Figure 6c presents the permeance data from Figure 6a against the reciprocal of the dry membrane thickness. These data roughly form a straight line at low reciprocal thickness, matching the scaling predicted by eqn. 8, but deviate at high reciprocal thickness. All three presentations of the data show systematic positive deviations from the best-fit homogeneous properties (dashed lines) at low thickness, indicating that the thinnest films are not as tightly cross-linked as their thicker counterparts.

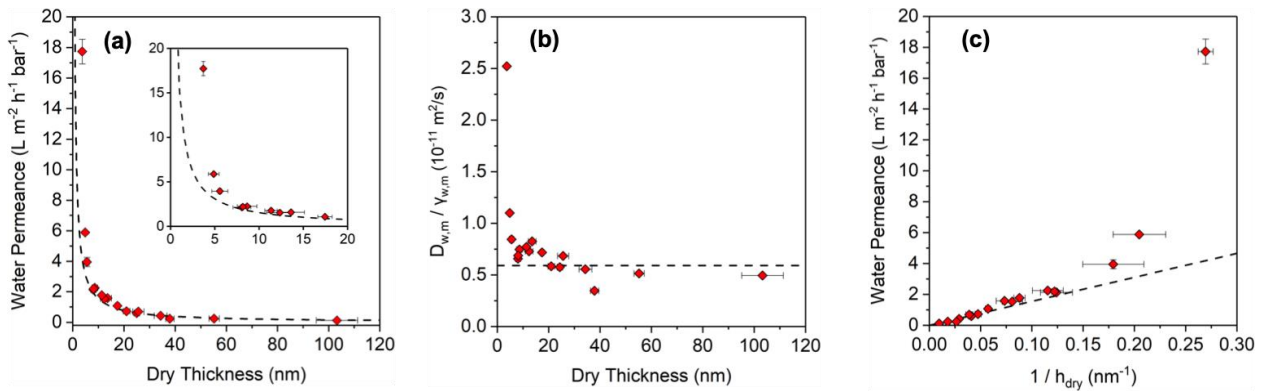


Figure 6. (a) Best fit of the SD model (eqn. 8) with homogeneous membrane properties to the measured water permeance, corresponding to $D_{w,m} / \gamma_{w,m} = 5.9 \times 10^{-12}$ m²/s. Inset graph shows the same data but only for films thinner than 20 nm to emphasize deviations from the model at low

thickness. (b) Water diffusion coefficient divided by the water activity coefficient for each film, via point-by-point fit to eqn. 8. The dashed line represents the best-fit value from (a). (c) Water permeance vs. reciprocal dry thickness. The dashed line represents the best-fit value from (a). The error bars represent one standard deviation of the data ($n = 3$ to 5), which is taken as the experimental uncertainty of the measurement. Some error bars are smaller than the symbols.

Prior studies have presented values for the diffusion coefficient of water in TMC/MPD networks, which often differ greatly from one another owing to the method of analysis. For example, a study on water absorption into TMC/MPD conducted via attenuated total reflection Fourier transform infrared spectroscopy (ATR-FTIR) reported $D_{w,m}$ varying from 3.3×10^{-13} m²/s to 2.2×10^{-12} m²/s for membranes with low acid content and high acid content, respectively.[34] A comparable value of $D_{w,m} = 3.8 \times 10^{-12}$ m²/s was reported in a water deswelling study conducted via poroelastic relaxation indentation (PRI).[35] In contrast a recent study on local molecular motion of water in TMC/MPD conducted via quasi-elastic neutron scattering (QENS) reported $D_{w,m} = 2.1 \times 10^{-9}$ m²/s,[36] essentially indistinguishable from the self-diffusion coefficient of bulk water $D_w = 2.3 \times 10^{-9}$ m²/s.[33] The systematic difference among these three prior studies and the present work appears to be the length scale over which molecular motion is considered. ATR-FTIR and PRI measurements yield the slowest diffusion coefficient and also probe diffusion over the longest length scales: ATR-FTIR probes water diffusion over the length scale of the film thickness and the penetration depth of the evanescent wave (≈ 10 μm and ≈ 1 μm respectively in the cited study[34]), while PRI probes water diffusion over the contact radius of the indenter tip (≈ 30 μm in the cited study[35]). QENS measurements yield the fastest diffusion coefficient, and sample motion over length scales on the order of one

to a few nanometers.[36] The present work falls in between these two extremes, reporting an intermediate diffusion coefficient corresponding to through-thickness diffusion across distances on the order of tens of nanometers. Taken as a series, these studies imply that the molecular mobility of water in TMC/MPD varies across several length scale regimes. Local motion is fast and nearly bulk-like, while effective motion across large distances is much more restricted likely due to the high tortuosity and presence of dead-ends in pathways conducive to long-range transport.

The fit of the data to a homogeneous SD model is reasonably good, except for substantial underestimations of the permeance at the lowest membrane thicknesses. To emphasize these thickness-dependent deviations from the SD model, each data point can be individually fitted to eqn. 6 as shown in Figure 6b. The quantity $D_{w,m} / \gamma_{w,m}$ shows a clear downward trend with increasing thickness, indicating that as mLbL deposition progresses to higher cycle count the membranes not only become thicker but also on average more restrictive to the motion of water molecules, thermodynamically less favorable for water partitioning, or both. A complementary phenomenon was previously reported by Chan and Lee[32] for swelling in membranes of the same chemistry and preparation technique, where the swelling ratio $\alpha = h_{\text{swollen}}/h_{\text{dry}}$ monotonically decreased with dry thickness.

Transport of salt can be modeled using comparable analysis, beginning with eqn. 5. Assume again that the NaCl activity coefficient in the feed and in the permeate is equal to unity. Owing to the large molar volume of the salt ions, the exponential term in eqn. 5 is near zero and accordingly the flux of salt has been observed to depend very weakly on pressure.[10] Salt flux is thus given by,

$$J_s \approx \frac{D_{s,m}}{\gamma_{s,m} h_m} (c_{s,f} - c_{s,p}) \quad (9)$$

The feed NaCl concentration, $c_{s,f}$, is recalculated at each time of collection, based on the total volumes and concentrations of the collected permeate solution. The calculated quotient of the membrane diffusion coefficient and the membrane activity coefficient ($D_{s,m} / \gamma_{s,m}$) for NaCl is shown in Figure 7 for each tested dry film thickness, as determined via the measured solution permeance and salt rejection for each membrane. Salt transport varies dramatically across the thinnest films in the series, with $D_{s,m} / \gamma_{s,m}$ declining by 3 orders of magnitude from a thickness of 4 nm to a thickness of 10 nm. However, above a film thickness of ≈ 15 nm salt transport abruptly becomes independent of thickness with $D_{s,m} / \gamma_{s,m}$ stabilizing to a constant value. These trends imply that the network structure and concentration of polar functional groups in mLbL films evolve dramatically over the first few dozen deposition cycles, but upon reaching this critical thickness a sufficiently tightly cross-linked barrier layer has formed to effectively exclude the passage of hydrated salt. Once formed, the properties of this barrier layer do not continue to evolve as the film grows thicker.

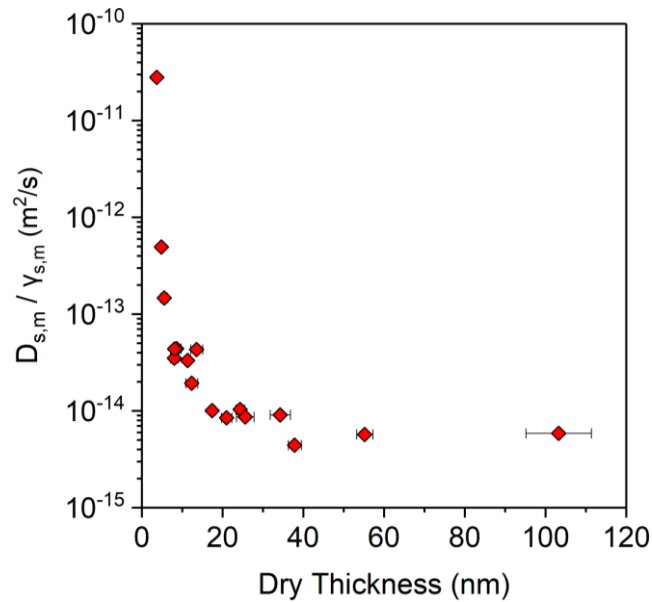


Figure 7. NaCl diffusion coefficient divided by the NaCl activity coefficient for each film, via point-by-point fit to eqn. 9. The error bars represent one standard deviation of the data ($n = 3$ to 5), which is taken as the experimental uncertainty of the measurement. Some error bars are smaller than the symbols.

3.4. Multi-Layer Solution-Diffusion

To explain the observed thickness dependence for water permeance and water swelling, we propose a depth-heterogeneous growth model during mLbL deposition. Suppose that freshly deposited monomer initially reacts to incomplete conversion, forming a relatively loose network with a low cross-link density while leaving behind a high population of unreacted functional groups. Only upon subsequent depositions can additional monomer can diffuse into and back-fill the pre-existing network as it swells in good solvent; vapor-swelling measurements show a swelling ratio of 1.25 for mLbL PA in toluene. This back filling continues until the network within the interior of the film becomes sterically saturated at a high cross-link density. This type of growth pattern is consistent with the trends in salt transport vs. film thickness shown in Figure 7, in which the membranes become increasingly impermeable to NaCl as the PA network tightens at low deposition cycle count, but salt transport stabilizes once the film interior has become saturated and the cross-link density cannot increase any further.

In this model, since subsequent depositions also polymerize fresh monomer onto the top of the growing film, a loose network layer at the free surface is continuously regenerated. We expect this surface layer to exhibit a continuous gradient in material properties, with the most lightly cross-linked network at the surface (high $D_{w,m}$ and low $\gamma_{w,m}$) approaching the tightly cross-linked network of the interior (low $D_{w,m}$ and high $\gamma_{w,m}$) with increasing depth. This type of

structure is analogous to the depth-heterogeneous morphology that naturally arises from a diffusion-controlled process like IP,[29,30] but here it arises due to the cyclic delivery of individual monomer species during a step-wise and repeated deposition process and is characterized by a thick dense layer beneath a thin loose layer, rather than the inverse geometry (a thin, dense skin layer with a thick, loose protuberance layer) for IP.

The SD model can be readily applied to this type of multi-layer structure, where the membrane properties are laterally homogeneous but vary through-thickness along the axis of mass transport. This is done by dividing the membrane into a number of homogeneous slabs in contact with each other, each at the feed pressure; a smooth gradient in properties can then be established by arranging many thin layers of slightly differing properties in a staircase approximation. The model formulation begins with Fick's law and the same definition of the chemical potential invoked for the single-layer model (eqns. 2 and 3). Eqn. 4 applies within each homogeneous layer n , and mass conservation requires that the fluxes $J_{i,n}$ are equal for each of the N total layers at steady state. Here, we also substitute each layer's dry thickness with an estimate of the thickness in the swollen state. Assuming that swelling in a slow transport process is always close to equilibrium,

$$\frac{h_{dry}}{h_{swollen}} \approx 1 - \frac{\gamma_{w,f} c_{w,f}}{\gamma_{w,m}} \quad (10)$$

The SD model assumes species equilibrium across each interface. At the feed interface with the first membrane layer ($n = 1$),

$$\gamma_{i,1} c_{i,1,hi} = \gamma_{i,f} c_{i,f} \quad (11)$$

At each subsequent internal interface between membrane layer n and layer $n + 1$,

$$\gamma_{i,n} c_{i,n,lo} = \gamma_{i,n+1} c_{i,n+1,hi} \quad (12)$$

Finally, at the permeate interface with layer $n = N$,

$$\gamma_{i,N} c_{i,N,lo} = \gamma_{i,p} c_{i,p} e^{-v_i \Delta P / (RT)} \quad (13)$$

Substitution of eqn. 4 and eqns. 10 – 13, with the condition that the fluxes across each layer must be equal, generates $(N - 1)$ coupled linear equations that can be solved simultaneously by matrix inversion (see the Supporting Information for the formulation of the flux model and for the numerical fitting methodology).

With the multi-layer SD model described, we proceed by assuming a form for the profiles of $D_{w,m}$ and $\gamma_{w,m}$ as a function of depth into the membrane. Here, we appeal to the above depth-heterogeneous growth model that we hypothesize is occurring during the mLbL process. Suppose for simplicity that the thickness and properties of the loose gradient layer at the surface of the mLbL membranes are independent of the total membrane thickness, so long as the total membrane is thicker than the gradient layer. That is, all sufficiently thick membranes have the same loose layer at their surface, characterized by the same gradients in $D_{w,m}$ and $\gamma_{w,m}$ and penetrating the same characteristic distance h_{loose} into the membrane, with the remaining bulk of the membrane with thickness $h_{dense} = h_{total} - h_{loose}$ having the properties of a sterically-saturated, highly cross-linked network $D_{w,dense}$ and $\gamma_{w,dense}$. Membranes thinner than h_{loose} are then taken to consist entirely of the loose material, truncated to the membrane's total thickness. An illustration of this depth-profiling scheme is shown in Figure 8.

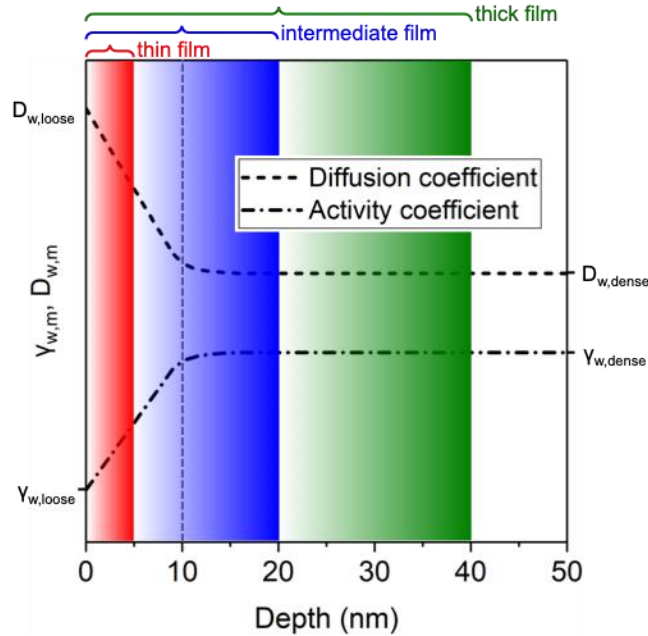


Figure 8. Hypothetical example of a membrane depth profile, for water diffusion coefficient ($D_{w,m}$) and water activity coefficient ($\gamma_{w,m}$). $D_{w,m}$ and $\gamma_{w,m}$ transition from a “loose” surface value to a “dense” saturated value over a characteristic length; $h_{\text{loose}} \approx 10$ nm in this example, shown by the vertical dashed line. Each of the three membranes shown (thin, intermediate, and thick) shares the same depth profile, truncated from the surface (depth = 0 nm) to that membrane’s maximum thickness.

The simplest useful depth profile would allow the water activity coefficient, $\gamma_{w,m}$, to vary from a low value at the membrane surface (corresponding to a higher swelling ratio) to a higher value deep in the membrane, in order to capture the thickness-dependent swelling data reported by Chan and Lee,[32] while assuming a constant water diffusion coefficient, $D_{w,m}$, throughout. This approach introduces the fewest free parameters into the model while still allowing for thickness-dependent evolution of the observed properties. We allow the single value of $D_{w,m}$ to

vary, along with the thicknesses and water activity coefficients of a stack of homogeneous slabs to generate a smooth, continuous profile for $\gamma_{w,m}(z)$.

The same model $\gamma_{w,m}(z)$ profile is used to simultaneously fit both the water permeance vs. dry thickness data series reported here, and the swelling ratio (extrapolated to water activity 1) vs. dry thickness series reported in ref. [32]. A full description of the models and the fitting methodology is provided in the Supporting Information. Briefly, the model water permeance is determined via eqn. 4 and eqns. 10 – 13, and the model swelling ratio is determined via eqn. 10 by calculating the swollen thickness of each layer and observing,

$$\alpha = \frac{\sum h_{swollen}}{\sum h_{dry}} \quad (14)$$

To facilitate simultaneous modeling of water permeance during pressurized operation and water swelling under ambient conditions using the same profile, it is assumed that $\gamma_{w,m}$ is independent or weakly dependent on pressure.

The best-fit water activity coefficient profile is shown in Figure 9c, along with the corresponding model curves for water permeance (9a) and water swelling (9b). Here the best-fit single value for the diffusion coefficient is $D_{w,m} = 6.7 \times 10^{-11} \text{ m}^2/\text{s}$, very close to the value estimated by the single-layer SD model fit to the data. The water activity coefficient ($\gamma_{w,m}$) varies from 4.5 at the surface to 12.9 in limit of high depth (corresponding to a variation in local swelling from 29 % to 8 %), over a characteristic depth of 10 nm. The quality of the fit for both data sets is very good, even without allowing for any depth-dependent variations in water mobility.

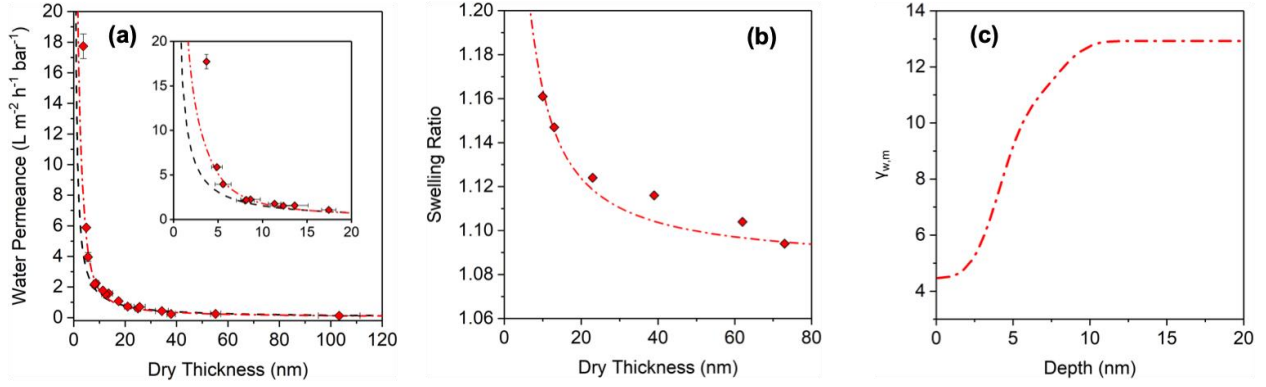


Figure 9. (a) Best fit of the multi-layer SD model (eqns. 4 and 10 – 13) with depth-variable water activity coefficient and constant $D_{w,m} = 6.7 \times 10^{-11}$ m²/s (red dash-dot curve). For comparison, the best fit to the single-layer SD model (eqn. 8) is also shown (black dash curve). Inset graph shows the same data, but only films thinner than 20 nm. The error bars represent one standard deviation of the data ($n = 3$ to 5), which is taken as the experimental uncertainty of the measurement. Some error bars are smaller than the symbols. (b) Best fit of the multi-layer swelling model (sum of eqn. 10 for each layer) to the data presented in ref. [32], extrapolated to water activity 1. (c) Water activity coefficient depth profile used to fit graphs (a) and (b).

However, the fixed- $D_{w,m}$ model still significantly under-predicts the water permeance for the thinnest membrane in the series. It is unclear how much weight should be attributed to a single data point, particularly the film with the lowest thickness and therefore the most susceptible to small perforations during the transfer process or during pressurization. With this caveat, the flux model can be modestly improved by allowing the diffusion coefficient to vary along with the activity coefficient. The fitting procedure is analogous to that used to generate the model in Figure 9, only now each layer slab is allowed to take an independent value of $\gamma_{w,m}$ and $D_{w,m}$. Analogously to the model above, the same set of $\gamma_{w,m}(z)$ and $D_{w,m}(z)$ profiles is used to simultaneously fit both the water permeance vs. dry thickness data series, and the swelling ratio

(extrapolated to water activity 1) vs. dry thickness series. The best-fit profiles are shown in Figure 10c, along with the corresponding model curves for water permeance (10a) and water swelling (10b). For comparison, the fixed- $D_{w,m}$ model and the single-layer SD model are also shown in Figure 10.

This complex profile has the diffusion coefficient vary from $2.8 \times 10^{-10} \text{ m}^2/\text{s}$ at the surface to $6.3 \times 10^{-11} \text{ m}^2/\text{s}$ in the limit of high depth, and the activity coefficient vary from 4.2 at the surface to 12.2 in the limit of high depth (corresponding to a variation in local swelling from 31 % to 9 %). This gradient layer for this profile is thinner than the profile corresponding to a fixed $D_{w,m}$: membrane properties transition from their surface values to their dense values in slightly under 5 nm, rather than 10 nm in the case shown in Figure 9. In either case, the models imply the presence of a very thin skin layer arising from the mLbL deposition method, albeit one with substantially different network behavior from the rest of the membrane and thus capable of generating measurable thickness-dependent trends in key macroscopic properties.

The multi-layer SD model derived here is general in nature and can be readily applied to any non-porous layered structure of uniform thickness. The type of analysis presented above could therefore be performed for any number of membrane transport systems, either composed of multiple discrete layers or exhibiting smooth gradients in properties.

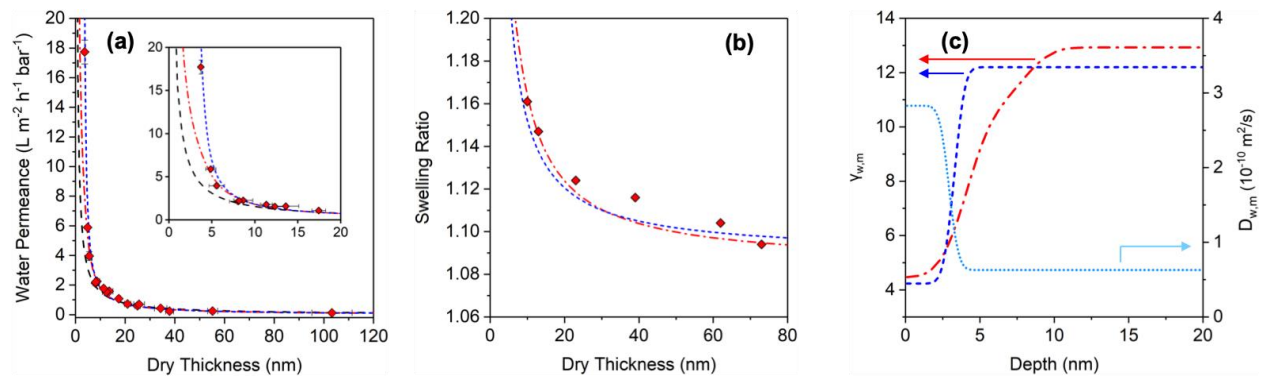


Figure 10. (a) Best fit of the multi-layer SD model (eqns. 4 and 10 – 13) with depth-variable water activity coefficient and depth-variable water diffusion coefficient (blue short-dash curve). Also shown are the best fits to the variable- $\gamma_{w,m}$, constant- $D_{w,m}$ model (red dash-dot curve) and to the single-layer SD model (eqn. 8; black dash curve). Inset graph shows the same data, but only films thinner than 20 nm. The error bars represent one standard deviation of the data ($n = 3$ to 5), which is taken as the experimental uncertainty of the measurement. Some error bars are smaller than the symbols. (b) Best fit of the multi-layer swelling model (blue short-dash curve) to the data presented in ref. [32], extrapolated to water activity 1. The best fit to the constant- $D_{w,m}$ model model is also shown (red dash-dot curve) (c) Profiles used to fit graphs (a) and (b). The blue dash curved represent the model with variable $\gamma_{w,m}$ and $D_{w,m}$; the red dash-dot curve represents the model with constant $D_{w,m}$.

4. Conclusions

In this work, we have presented the thickness-dependent transport of water and hydrated NaCl in a series of TMC-MPD membranes prepared via mLbL deposition. These mLbL films exhibit low surface roughness and well-defined, uniform thickness, and are thus amenable to quantitative analysis via the SD model. This approach reveals continuous evolution in the diffusion coefficient and activity coefficient of both water and salt with increasing film thickness, suggesting that thicker mLbL films have a higher average network density and are thus more restrictive to transport than thinner mLbL films.

The water diffusion coefficient is of particular interest for the design of high-flux RO membranes. For the thickest TMC-MPD mLbL films, $D_{w,m}$ approaches a constant value of approximately 6.5×10^{-11} m²/s. This value falls between a higher value previously reported for

the same material by QENS,[36] and lower values previously reported for the same material by ATR-FTIR[34] and PRI.[35] To explain these discrepancies present in the literature, we have proposed that the effective diffusion coefficient is length-scale dependent: local motion is fast and nearly bulk-like, while long-range motion is restricted due to the effects of tortuosity and dead-ends in the network pathways available for transport. Our measurement method, through-thickness solution flux measurements, probes a length scale between the nanometer-scale QENS method and the micron-scale ATR-FTIR and PRI methods, and therefore corresponds to an intermediate effective diffusivity.

Within our series of mLbL films, we explain the thickness-dependence of the water diffusion and activity coefficients as a surface effect. We have derived and presented a multi-layer formulation of the SD model, which reveals the presence of a (5 to 10) nm layer of material at the film surface. Compared to the film interior, this surface layer exhibits greater water swelling ($\approx 30\%$ at the surface compared to slightly less than 10% for the interior) and possibly enhanced water mobility, and can be physically understood as a region of lighter cross-linking and higher concentration of unreacted, polar functional groups arising from the stepwise mLbL deposition process. While not directly observed, the presence of such a surface layer would offer an explanation for both the thickness-dependent permeance and swelling of mLbL PA membranes, as a (5 to 10) nm layer dominates the average behavior of a very thin film but becomes an insignificant fraction of a much thicker film.

The existence of this loosely cross-linked surface layer may also explain the variations of NaCl rejection with changes in membrane thickness. There is little evidence of porosity in even the thinnest films, yet for films thinner than about 8 nm rejection is poor and highly sensitive to small changes in thickness. Between 8 nm and 15 nm, rejection stabilizes from $\approx 88\%$ at 8 nm to

$\approx 97\%$ at 15 nm. Finally, rejection is essentially independent of thickness and the material parameter governing salt transport, $D_{s,m} / \gamma_{s,m}$, reaches a constant value above 15 nm. We cannot definitively rule out the possibility of membrane rupture for the thinnest films based on the data presented here. However, the water permeance even of the thinnest membrane in the series is more than a factor of 30 lower than that of the bare PAN support, requiring that the large majority if not all of the membrane's surface area has remained intact. Instead, the appearance of the transition regime for salt rejection around film thicknesses of 8 nm is in striking coincidence with the prediction of the multi-layer solution-diffusion model, where a loosely cross-linked layer occupies the uppermost (5 to 10) nm of the mLbL membranes. According to the depth profile proposed here, films thinner than that critical thickness consist entirely of this lightly cross-linked PA, such that their network structures are too loose and swell too much in aqueous solution to exclude hydrated salt ions. Therefore, the onset of efficient salt rejection corresponds to the first appearance of a layer of maximally cross-linked PA beneath the surface layer, even though this sterically saturated layer may be no more than a few nanometers thick.

If true, this association of efficient NaCl rejection with the formation of an extremely thin though tightly cross-linked dense layer is a valuable design rule for the optimization of PA TFC membranes. All that is needed to efficiently exclude hydrated NaCl is ≈ 5 nanometers of dense PA network, less even than the ≈ 20 nm skin layers proposed to form in the IP process,[29,30] as long as those few nanometers are close to the maximum sterically-achievable cross-link density for the TMC/MPD chemistry. By thus reducing the thickness of the active layer to the lower limit consistent with high salt rejection, the energy costs of operation can be minimized while retaining RO performance. Membranes meeting these criteria may be achievable by methods

such as molecular layer deposition,[37–39] ideally on support materials with rough or nano-structured surfaces to maximize the available surface area of the active layer.

A topic for future study may involve methods to suppress or eliminate the formation of a loose surface layer in mLbL films, in order to improve salt rejection in this thickness regime where water permeance is highest. One candidate method might utilize a finishing or capping step, in which the mLbL process ends with deposition of a different monomer species to react with any remaining functional groups at the surface. For example, the final TMC deposition could be followed with a high-functionality amine (*e.g.* branched polyethylenimine) to generate a high surface cross-link density by consuming residual acid chloride groups.

5. References

- [1] M. Elimelech, W.A. Phillip, The Future of Seawater Desalination: Energy, Technology, and the Environment, *Science*. 333 (2011) 712–717. <https://doi.org/10.1126/science.1200488>.
- [2] G.M. Geise, H.-S. Lee, D.J. Miller, B.D. Freeman, J.E. McGrath, D.R. Paul, Water purification by membranes: The role of polymer science, *J. Polym. Sci. B Polym. Phys.* 48 (2010) 1685–1718. <https://doi.org/10.1002/polb.22037>.
- [3] K.P. Lee, T.C. Arnot, D. Mattia, A review of reverse osmosis membrane materials for desalination—Development to date and future potential, *J. Memb. Sci.* 370 (2011) 1–22. <https://doi.org/10.1016/j.memsci.2010.12.036>.
- [4] C.A. Schlosser, K. Strzepek, X. Gao, C. Fant, É. Blanc, S. Paltsev, H. Jacoby, J. Reilly, A. Gueneau, The future of global water stress: An integrated assessment: SCHLOSSER ET AL., *Earth's Future*. 2 (2014) 341–361. <https://doi.org/10.1002/2014EF000238>.
- [5] J.E. Cadotte, R.S. King, R.J. Majerle, R.J. Petersen, Interfacial Synthesis in the Preparation of Reverse Osmosis Membranes, *J. Macromol. Sci. Part A-Chem.* 15 (1981) 727–755. <https://doi.org/10.1080/00222338108056764>.
- [6] R.J. Petersen, J.E. Cadotte, Thin Film Composite Reverse Osmosis Membranes, in: M.C. Porter (Ed.), *Handbook of Industrial Membrane Technology*, Noyes Publications, New Jersey, 1990: pp. 307–348.
- [7] V. Freger, Nanoscale Heterogeneity of Polyamide Membranes Formed by Interfacial Polymerization, *Langmuir*. 19 (2003) 4791–4797. <https://doi.org/10.1021/la020920q>.
- [8] O. Coronell, B.J. Mariñas, D.G. Cahill, Depth Heterogeneity of Fully Aromatic Polyamide Active Layers in Reverse Osmosis and Nanofiltration Membranes, *Environ. Sci. Technol.* 45 (2011) 4513–4520. <https://doi.org/10.1021/es200007h>.

- [9] K. Li, S. Li, L. Liu, W. Huang, Y. Wang, C. Yu, Y. Zhou, Molecular dynamics simulation studies of the structure and antifouling performance of a gradient polyamide membrane, *Phys. Chem. Chem. Phys.* 21 (2019) 19995–20002. <https://doi.org/10.1039/C9CP03798E>.
- [10] J.G. Wijmans, R.W. Baker, The solution-diffusion model: a review, *J. Memb. Sci.* 107 (1995) 1–21. [https://doi.org/10.1016/0376-7388\(95\)00102-I](https://doi.org/10.1016/0376-7388(95)00102-I).
- [11] D. Paul, Reformulation of the solution-diffusion theory of reverse osmosis, *J. Memb. Sci.* 241 (2004) 371–386. <https://doi.org/10.1016/j.memsci.2004.05.026>.
- [12] A.K. Ghosh, B.-H. Jeong, X. Huang, E.M.V. Hoek, Impacts of reaction and curing conditions on polyamide composite reverse osmosis membrane properties, *J. Memb. Sci.* 311 (2008) 34–45. <https://doi.org/10.1016/j.memsci.2007.11.038>.
- [13] P.M. Johnson, J. Yoon, J.Y. Kelly, J.A. Howarter, C.M. Stafford, Molecular layer-by-layer deposition of highly crosslinked polyamide films, *J. Polym. Sci. B Polym. Phys.* 50 (2012) 168–173. <https://doi.org/10.1002/polb.23002>.
- [14] S. Karan, Z. Jiang, A.G. Livingston, Sub-10 nm polyamide nanofilms with ultrafast solvent transport for molecular separation, *Science*. 348 (2015) 1347–1351.
- [15] Z. Jiang, S. Karan, A.G. Livingston, Water Transport through Ultrathin Polyamide Nanofilms Used for Reverse Osmosis, *Adv. Mater.* 30 (2018) 1705973. <https://doi.org/10.1002/adma.201705973>.
- [16] J.-E. Gu, S. Lee, C.M. Stafford, J.S. Lee, W. Choi, B.-Y. Kim, E.P. Chan, J.Y. Chung, J. Bang, J.-H. Lee, Molecular Layer-by-Layer Assembled Thin-Film Composite Membranes for Water Desalination, *Adv. Mater.* 25 (2013) 4778–4782.
- [17] J.-E. Gu, J.S. Lee, S.-H. Park, I.T. Kim, E.P. Chan, Y.-N. Kwon, J.-H. Lee, Tailoring interlayer structure of molecular layer-by-layer assembled polyamide membranes for high separation performance, *Appl. Surf. Sci.* 356 (2015) 659–667. <https://doi.org/10.1016/j.apsusc.2015.08.119>.
- [18] P. Manna, A. Tiraferri, M. Sangermano, R. Bernstein, R. Kasher, Stepwise synthesis of oligoamide coating on a porous support: Fabrication of a membrane with controllable transport properties, *Separation and Purification Technology*. 213 (2019) 11–18. <https://doi.org/10.1016/j.seppur.2018.12.014>.
- [19] E.P. Chan, J.-H. Lee, J.Y. Chung, C.M. Stafford, An automated spin-assisted approach for molecular layer-by-layer assembly of crosslinked polymer thin films, *Review of Scientific Instruments*. 83 (2012) 114102. <https://doi.org/10.1063/1.4767289>.
- [20] S.-B. Kwon, J.S. Lee, S.J. Kwon, S.-T. Yun, S. Lee, J.-H. Lee, Molecular layer-by-layer assembled forward osmosis membranes, *Journal of Membrane Science*. 488 (2015) 111–120. <https://doi.org/10.1016/j.memsci.2015.04.015>.
- [21] W. Choi, J.-E. Gu, S.-H. Park, S. Kim, J. Bang, K.-Y. Baek, B. Park, J.S. Lee, E.P. Chan, J.-H. Lee, Tailor-Made Polyamide Membranes for Water Desalination, *ACS Nano*. 9 (2015) 345–355. <https://doi.org/10.1021/nn505318v>.
- [22] The appropriate SI unit for pressure is MPa. However, the conventional notation, bar, has been employed for this publication as it is the accepted unit in the field.
- [23] T.P. Liyana-Arachchi, J.F. Sturnfield, C.M. Colina, Ultrathin Molecular-Layer-by-Layer Polyamide Membranes: Insights from Atomistic Molecular Simulations, *J. Phys. Chem. B*. 120 (2016) 9484–9494. <https://doi.org/10.1021/acs.jpcc.6b02801>.
- [24] W. Ying, R. Kumar, M. Herzberg, R. Kasher, Diminished Swelling of Cross-Linked Aromatic Oligoamide Surfaces Revealing a New Fouling Mechanism of Reverse-Osmosis

- Membranes, *Environ. Sci. Technol.* 49 (2015) 6815–6822.
<https://doi.org/10.1021/es504325d>.
- [25] S.A. Sundet, Morphology of the rejecting surface of aromatic polyamide membranes for desalination, *J. Memb. Sci.* 76 (1993) 175–183. [https://doi.org/10.1016/0376-7388\(93\)85215-I](https://doi.org/10.1016/0376-7388(93)85215-I).
- [26] R. Nadler, S. Srebnik, Molecular simulation of polyamide synthesis by interfacial polymerization, *Journal of Membrane Science.* 315 (2008) 100–105.
<https://doi.org/10.1016/j.memsci.2008.02.023>.
- [27] M.T.M. Pendergast, J.M. Nygaard, A.K. Ghosh, E.M.V. Hoek, Using nanocomposite materials technology to understand and control reverse osmosis membrane compaction, *Desalination.* 261 (2010) 255–263. <https://doi.org/10.1016/j.desal.2010.06.008>.
- [28] Y.A. Hussain, M.H. Al-Saleh, A viscoelastic-based model for TFC membranes flux reduction during compaction, *Desalination.* 344 (2014) 362–370.
<https://doi.org/10.1016/j.desal.2014.04.010>.
- [29] H. Yan, X. Miao, J. Xu, G. Pan, Y. Zhang, Y. Shi, M. Guo, Y. Liu, The porous structure of the fully-aromatic polyamide film in reverse osmosis membranes, *J. Memb. Sci.* 475 (2015) 504–510. <https://doi.org/10.1016/j.memsci.2014.10.052>.
- [30] V. Freger, Swelling and Morphology of the Skin Layer of Polyamide Composite Membranes: An Atomic Force Microscopy Study, *Environ. Sci. Technol.* 38 (2004) 3168–3175. <https://doi.org/10.1021/es034815u>.
- [31] S.-Y. Kwak, S.G. Jung, Y.S. Yoon, D.W. Ihm, Details of surface features in aromatic polyamide reverse osmosis membranes characterized by scanning electron and atomic force microscopy, *J. Polym. Sci., Part B: Polym. Phys.* 37 (1999) 1429–1440.
- [32] E.P. Chan, S.C. Lee, Thickness-dependent swelling of molecular layer-by-layer polyamide nanomembranes, *J. Polym. Sci. Part B: Polym. Phys.* 55 (2017) 412–417.
<https://doi.org/10.1002/polb.24285>.
- [33] M. Holz, S.R. Heil, A. Sacco, Temperature-dependent self-diffusion coefficients of water and six selected molecular liquids for calibration in accurate 1H NMR PFG measurements, *Phys. Chem. Chem. Phys.* 2 (2000) 4740–4742. <https://doi.org/10.1039/b005319h>.
- [34] Y. Jin, W. Wang, Z. Su, Spectroscopic study on water diffusion in aromatic polyamide thin film, *Journal of Membrane Science.* 379 (2011) 121–130.
<https://doi.org/10.1016/j.memsci.2011.05.055>.
- [35] E.P. Chan, Deswelling of ultrathin molecular layer-by-layer polyamide water desalination membranes, *Soft Matter.* 10 (2014) 2949. <https://doi.org/10.1039/c4sm00088a>.
- [36] E.P. Chan, B.R. Frieberg, K. Ito, J. Tarver, M. Tyagi, W. Zhang, E.B. Coughlin, C.M. Stafford, A. Roy, S. Rosenberg, C.L. Soles, Insights into the Water Transport Mechanism in Polymeric Membranes from Neutron Scattering, *Macromolecules.* 53 (2020) 1443–1450.
<https://doi.org/10.1021/acs.macromol.9b02195>.
- [37] A. Kubono, N. Okui, K. Tanaka, S. Umemoto, T. Sakai, Highly oriented polyamide thin films prepared by vapor deposition polymerization, *Thin Solid Films.* 199 (1991) 385–393.
- [38] N.M. Adamczyk, A.A. Dameron, S.M. George, Molecular Layer Deposition of Poly(*p*-phenylene terephthalamide) Films Using Terephthaloyl Chloride and *p*-Phenylenediamine, *Langmuir.* 24 (2008) 2081–2089. <https://doi.org/10.1021/la7025279>.
- [39] Q. Peng, K. Efimenko, J. Genzer, G.N. Parsons, Oligomer Orientation in Vapor-Molecular-Layer-Deposited Alkyl-Aromatic Polyamide Films, *Langmuir.* 28 (2012) 10464–10470.
<https://doi.org/10.1021/la3017936>.

Supplemental Materials for

Thickness-Dependent Permeance of Molecular Layer-By-Layer Polyamide Membranes

William D. Mulhearn, Vladimir P. Oleshko, Christopher M. Stafford

Materials Science and Engineering Division, National Institute of Standards and Technology,

Gaithersburg, MD 20899, USA

S1. mLbL Film Growth Rate

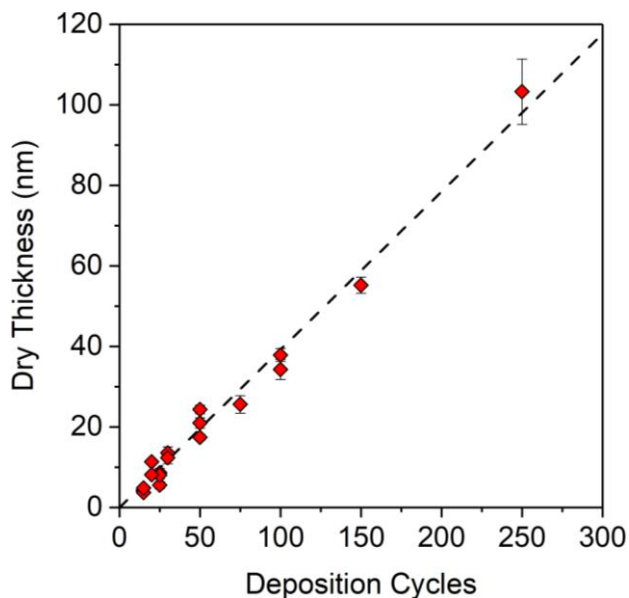


Figure S1. Polyamide mLbL dry film thickness vs. number of deposition cycles. The dashed line corresponds to the best linear fit to the data, with a slope of (0.39 ± 0.02) nm/cycle; the uncertainty corresponds to a 95% confidence interval. The error bars represent one standard deviation of the data ($n = 3$ to 5), which is taken as the experimental uncertainty of the measurement. Some error bars are smaller than the symbols.

S2. Tabulated Water Permeance and NaCl Rejection vs. Thickness

Dry Thickness (nm)	Permeance (L m ⁻² h ⁻¹ bar ⁻¹)	NaCl Rejection (%)
3.7	17.7	4.1
4.9	5.9	50.5
5.6	4.0	72.2
8.1	2.1	89.1
8.2	2.2	87.3
8.6	2.3	88.1
11.4	1.8	90.9
12.4	1.5	94.2
13.6	1.6	89.0
17.4	1.1	96.8
21.0	0.72	96.7
24.4	0.60	95.8
25.6	0.70	97.1
34.3	0.42	96.2
37.9	0.24	97.0
55.2	0.24	98.0
103	0.12	97.9

S3. Formulation of the Multi-Layer Solution-Diffusion Model

Flux through a multi-layer structure in which each individual layer conforms to the solution-diffusion (SD) model can be described as follows. The flux of species of interest i through each layer n is given by,

$$J_{i,n} = \frac{D_{i,n}}{h_n} (c_{i,n,hi} - c_{i,n,lo}) \quad (S1)$$

where $D_{i,n}$ is the species diffusion coefficient in layer n , h_n is the layer thickness, and $c_{i,n,hi}$ and $c_{i,n,lo}$ are the molar species concentrations within the layer at the high-concentration interface

(*i.e.*, closest to the feed) and the low-concentration interface (*i.e.*, closest to the permeate), respectively. Assume species equilibrium across each interface. At the feed, *f*, interface with membrane layer $n = 1$,

$$\gamma_{i,1} c_{i,1,hi} = \gamma_{i,f} c_{i,f} \quad (\text{S2})$$

where γ_i is the activity coefficient of species i . At each internal interface between membrane layer n and layer $n + 1$,

$$\gamma_{i,n} c_{i,n,lo} = \gamma_{i,n+1} c_{i,n+1,hi} \quad (\text{S3})$$

At the permeate, *p*, interface with layer $n = N$,

$$\gamma_{i,N} c_{i,N,lo} = \gamma_{i,p} c_{i,p} e^{-v_i \Delta P / (RT)} \quad (\text{S4})$$

where v_i is the molar volume ($v_w = 1.8 \times 10^{-5} \text{ m}^3/\text{mol}$ for water), ΔP is the pressure difference between the feed and the permeate, R is the gas constant, and T is the absolute temperature. At steady state, mass conservation requires that the $J_{i,n}$ be equal for each of the N layers. At the first internal interface, between layer 1 and layer 2, substitution of eqns. S1, S2, and S3 gives,

$$\left(\frac{D_{i,1}}{h_1} + \frac{D_{i,2} \gamma_{i,1}}{h_2 \gamma_{i,2}} \right) c_{i,1,lo} + \left(-\frac{D_{i,2}}{h_2} \right) c_{i,2,lo} = \frac{D_{i,1} \gamma_{i,f}}{h_1 \gamma_{i,1}} c_{i,f} \quad (\text{S5})$$

At internal interfaces between layer n and layer $n + 1$, where $n = 2, 3, \dots, (N - 2)$, substitution of eqns. S1 and S3 gives,

$$\left(-\frac{D_{i,n} \gamma_{i,n-1}}{h_n \gamma_{i,n}} \right) c_{i,n-1,lo} + \left(\frac{D_{i,n}}{h_n} + \frac{D_{i,n+1} \gamma_{i,n}}{h_{n+1} \gamma_{i,n+1}} \right) c_{i,n,lo} + \left(-\frac{D_{i,n+1}}{h_{n+1}} \right) c_{i,n+1,lo} = 0 \quad (\text{S6})$$

And finally, at the internal interface between layer $(N - 1)$ and layer N , substitution of eqns. S1, S3, and S4 gives,

$$\left(-\frac{D_{i,N-1} \gamma_{i,N-2}}{h_{N-1} \gamma_{i,N-1}} + \frac{D_{i,2} \gamma_{i,1}}{h_2 \gamma_{i,2}} \right) c_{i,N-2,lo} + \left(\frac{D_{i,N-1}}{h_{N-1}} + \frac{D_{i,N} \gamma_{i,N-1}}{h_N \gamma_{i,N}} \right) c_{i,N-1,lo} = \frac{D_{i,N} \gamma_{i,p}}{h_N \gamma_{i,N}} c_{i,p} e^{-v_i \Delta P / (RT)} \quad (\text{S7})$$

All quantities in eqns. S5 – S7 are either known or will be taken as adjustable parameters, except for the interior concentrations $c_{i,n,lo}$. For readability, we make the definitions,

$$f_1 \equiv \frac{D_{i,1} \gamma_{i,f}}{h_1 \gamma_{i,1}} c_{i,f} \quad (\text{S8})$$

$$p_N \equiv \frac{D_{i,N} \gamma_{i,p}}{h_N \gamma_{i,N}} c_{i,p} e^{-v_i \Delta P / (RT)} \quad (\text{S9})$$

$$x_{n,n+1} \equiv -\frac{D_{i,n} \gamma_{i,n-1}}{h_n \gamma_{i,n}} \quad (\text{S10})$$

$$y_{n,n+1} \equiv \frac{D_{i,n}}{h_n} + \frac{D_{i,n+1} \gamma_{i,n}}{h_{n+1} \gamma_{i,n+1}} \quad (\text{S11})$$

$$z_{n,n+1} \equiv -\frac{D_{i,n+1}}{h_{n+1}} \quad (\text{S12})$$

Eqns. S5 – S7 present $(N - 1)$ equations for the $(N - 1)$ unknowns (the $c_{i,n,lo}$ for $n = 1, 2, \dots, (N - 1)$). These equations can be written in matrix form,

$$\begin{bmatrix} y_{1,2} & z_{1,2} & 0 & & 0 & 0 \\ x_{2,3} & y_{2,3} & z_{2,3} & \dots & 0 & 0 \\ 0 & x_{3,4} & y_{3,4} & & 0 & 0 \\ & \vdots & & \ddots & & \\ 0 & 0 & 0 & \dots & y_{N-2,N-1} & z_{N-2,N-1} \\ 0 & 0 & 0 & \dots & x_{N-1,N} & y_{N-1,N} \end{bmatrix} \begin{bmatrix} c_{i,1,lo} \\ c_{i,2,lo} \\ c_{i,2,lo} \\ \vdots \\ c_{i,N-2,lo} \\ c_{i,N-1,lo} \end{bmatrix} = \begin{bmatrix} f_1 \\ 0 \\ 0 \\ \vdots \\ 0 \\ p_N \end{bmatrix} \quad (\text{S13})$$

The vector of the $c_{i,n,lo}$ values can be obtained by matrix inversion. The system flux is then calculated via eqn. S1 and any $c_{i,n,hi}$, $c_{i,n,lo}$ pair, for example,

$$J_i = \frac{D_{i,1}}{h_1} \left(\frac{\gamma_{i,f}}{\gamma_{i,1}} c_{i,f} - c_{i,1,lo} \right) \quad (\text{S14})$$

S3. Depth Profile Construction

Parameter-adjustable membrane depth profiles for the water activity coefficient, γ_w , and the water diffusion coefficient D_w , were generated as follows. We begin with three or four slabs, each characterized by an independent dry thickness h_{dry} (with the dry thickness of the final slab representing the dense material constrained such that the sum of thicknesses equals 120 nm, slightly thicker than the largest dry thickness among the experimental data points), an independent γ_w , and either an independent D_w or a shared D_w depending on the complexity of the

chosen model. These parameter sets were used to generate coarse, step-change functions of γ_w and D_w vs. dry depth. The coarse functions were smoothed via convolution with a Gaussian of characteristic width of 3 nm, to better simulate the gradual, continuous property variations expected of a real material. These smoothed functions were captured as a staircase approximation of 1000 discrete layers. Each experimental data point, corresponding to a membrane of $h_{dry} < 120$ nm, was then modeled by truncating the smoothed profiles up to the dry thickness of the corresponding membrane.

Before supplying these truncated profiles to the model (eqns. S8 – S14, which assume membrane thicknesses in the swollen state during operation), the thickness of each layer was corrected to account for near-equilibrium swelling,

$$h_{swollen} = h_{dry} / \left(1 - \frac{\gamma_{w,f} c_{w,f}}{\gamma_{w,n}} \right) \quad (\text{S15})$$

The swelling ratio of the membrane is then calculated as,

$$\alpha = \frac{\sum h_{swollen}}{\sum h_{dry}} \quad (\text{S16})$$

The adjustable parameters h_{dry} , γ_w , and D_w for each coarse slab were varied to generate the best fit to the experimental flux and swelling data. In all cases, the water activity coefficients of the feed and of the permeate were taken to be equal to 1.